Research Article | Vol. 13, No. 9 / 1 Sep 2022 / Biomedical Optics Express 4954
Biomedical Optics EXPRESS

Combined optical fluorescence microscopy and X-ray tomography reveals substructures in cell nuclei in 3D

ANDREW WITTMEIER,[1] MARTEN BERNHARDT,[1] ANNA-LENA ROBISCH,[1] CHIARA CASSINI,[1,2] MARKUS OSTERHOFF,[1] TIM SALDITT,[1,2] AND SARAH KÖSTER[1,2,*]

[1]*Institute for X-Ray Physics, University of Göttingen, Friedrich-Hund-Platz 1, 37077 Göttingen, Germany*
[2]*Cluster of Excellence "Multiscale Bioimaging: from Molecular Machines to Networks of Excitable Cells" (MBExC), University of Göttingen, Germany*
[*]*Sarah.Koester@phys.uni-goettingen.de*

Abstract: The function of a biological cell is fundamentally defined by the structural architecture of packaged DNA in the nucleus. Elucidating information about the packaged DNA is facilitated by high-resolution imaging. Here, we combine and correlate hard X-ray propagation-based phase contrast tomography and visible light confocal microscopy in three dimensions to probe DNA in whole cell nuclei of NIH-3T3 fibroblasts. In this way, unlabeled and fluorescently labeled substructures within the cell are visualized in a complementary manner. Our approach enables the quantification of the electron density, volume and optical fluorescence intensity of nuclear material. By joining all of this information, we are able to spatially localize and physically characterize both active and inactive heterochromatin, euchromatin, pericentric heterochromatin foci and nucleoli.

1. Introduction

DNA within mammalian cell nuclei stores genetic information, is densely packed, and spans length scales from about 2 nm to 1 µm, corresponding to double helices and individual chromosomes, respectively [1,2]. The structural architecture of packaged DNA on intermediate length scales defines the cell function and is thus of critical importance. Understanding the structure of DNA is facilitated by imaging, and imaging structures on these length scales requires high spatial resolution in three dimensions. X-ray imaging [3] and optical fluorescence microscopy [4] are two ideal techniques that satisfy this requirement and are at the same time highly complementary in the physical quantities they probe.

X-rays are sensitive to the electron density of matter and can be used to quantitatively image large structures without the invasive need for slicing or staining [5]. Indeed, novel soft X-ray microscopy and tomography methods are able to resolve subcellular structures, including subnuclear features such as nucleoli, at unprecedented resolution in 2D and 3D [6,7]. Previously, soft X-ray tomography (SXT) was employed to investigate active and inactive chromosomes in human amniotic cells [8]. The authors observed both types of chromosomes to occupy similar volumes while differing in surface area, suggesting the spatial arrangement of both types is similar. These findings were extended by combing SXT with cryogenic optical confocal tomography, thus enabling the topological arrangement of inactive chromosomes in mouse lymphoma cells to be visualized [9].

Complementary to these successful approaches, our work focuses on the use of hard X-rays. Here, we classify X-rays with an energy of 5 keV or above as "hard". There are a number of reasons why we have extended X-ray microscopy of cells from the classical water window to the hard X-ray regime. First, full-field images can easily be collected in this regime at the same

#462493 https://doi.org/10.1364/BOE.462493
Journal © 2022 Received 27 Apr 2022; revised 8 Jul 2022; accepted 27 Jul 2022; published 25 Aug 2022

Biomedical Optics EXPRESS

photon energy and instrument at which one also collects data from as X-ray fluorescence and X-ray diffraction (albeit in scanning), and we thus gain versatility for future directions. Second, the higher photon energy enables a significantly extended depth of focus. For the same lateral resolution, the numerical aperture can be reduced by a factor of 20 (8 keV versus 400 eV), and accordingly the maximum depth over which tomography works without distortions. Third, when performed in this regime, X-ray microscopy can be easily extended to tissues, which is very interesting from a biophysical perspective. Finally, it is for reasons of image contrast. For hard X-rays, X-ray absorption in unstained biological cells is almost negligible and the image contrast is governed almost exclusively by phase differences, which can be related to electron density differences in quantitative terms. In this work in particular, the analysis of the cellular nuclei builds upon this relationship.

Indeed, hard X-ray methods have been applied for studying DNA structures in the past. Early on, X-ray diffraction was used to show that the structure of chromatin fibers is based on repeating units of histone proteins [10]. Coherent diffraction imaging enabled the identification of various organelles, including the nucleus, in whole, unstained yeast spore cells [11]. Using hard X-ray propagation-based phase contrast tomography, unstained and unsliced *Deinococcus radiodurans* have been imaged [12]. The authors attributed characteristic dense regions on the order of 1.4 $g \cdot cm^{-3}$ to be DNA-rich regions. This work was subsequently extended by combining X-ray tomography with ptychography to quantitatively image unsliced and unstained *Deinococcus radiodurans* at a resolution of 50 nm [13]. The combination of ptychography and X-ray tomography was also used to map the 3D electron density of *Chlamydomonas* cells [14]. The authors identified the electron density of the nucleus to be 450 $e^- \cdot nm^{-3}$. The use of energies as high as 17 KeV enables a combination of X-ray propagation-based phase contrast tomography and powerful X-ray fluorescence tomography to identify and localize chemical elements within cells and nuclei [15].

Similarly, the combination of X-ray propagation-based phase contrast tomography and optical fluorescence imaging is particularly fruitful as the collected signal originates from different sources, i.e., the total electron density and specifically labeled structures. The data sets are complementary as each offers a quantitative contrast mode that probes different physical quantities. Both can, in a correlative manner, be applied to biomolecular assemblies and organelles within a single cell. The combination of 3D X-ray diffraction and 2D optical fluorescence has been used to image mammalian cell nuclei [16]. The authors quantified the average electron density of the nucleus and a nucleolus to be 440 $e^- \cdot nm^{-3}$ and 620 $e^- \cdot nm^{-3}$, respectively. By comparison to optical fluorescence micrographs, they identified specific regions within the nucleus as heterochromatin. We have investigated the actin network within a mouse heart muscle cell using a combination of X-ray in-line holography, scanning small-angle X-ray scattering (scanning SAXS) and 2D stimulated emission depletion (STED) microscopy [17]. From these data, we concluded that the orientations of actin filaments found in the holography and STED data coincide with the principal directions of anisotropic diffraction patterns.

Here, we extend the very successful combination of X-ray propagation-based phase contrast tomography and optical fluorescence, specifically confocal microscopy, to nuclei of mammalian cells. This combined approach enables us to image subnuclear structures using a minimal number of labeling probes while still maintaining access to quantitative density information. We measure the fluorescence intensity and electron density in a spatially resolved manner and determine the volume of the subnuclear structures. We show that by combining this complementary information we are able to identify and localize important nuclear structures – active and inactive heterochromatin, euchromatin, pericentric heterochromatin foci (PHFs) and nucleoli – in a quantitative manner, i.e., evaluating density information of the features. Thus, we present the results of a combined imaging technique that is widely applicable to biological and soft matter samples. Examples include virtually all types of biological cells and intracellular organelles, as

Biomedical Optics EXPRESS

well as polymer or hybrid materials. A prerequisite for the confocal imaging is the possibility of labeling the component of interest using fluorophores.

2. Materials and methods

2.1. Sample preparation

All experiments presented in this work are conducted on NIH-3T3 fibroblasts derived from Swiss albino mouse embryos [18]. This particular cell type was chosen for the present proof-of-concept study due to its wide availability in a large number of biology and biophysics labs, the extensive body of work by other researchers using complementary techniques available, and the high robustness of these cells. The cells are cultured in 25 cm^2 cell-culture flasks (Nunc A/S, Roskilde, Denmark) using high-glucose (4.5 $g \cdot mL^{-1}$) Dulbecco's Modified Eagle's Medium (DMEM, D6429, Sigma-Aldrich, Taufkirchen, Germany) supplemented with 10% ($^v/_v$) fetal bovine serum (F0804, Sigma-Aldrich) and 1% ($^v/_v$) penicillin-streptomycin. The cells are stored in a water-saturated cell incubator kept at 37 °C with 5% CO_2. Once the cells reach a confluency of ~ 80% they are detached from the flask via trypsin incubation (37 °C, 5% CO_2) for 150 s using 1 mL of 0.05% trypsin derived from porcine pancreas (Sigma-Aldrich). A silicon-rich nitride membrane (membrane size and thickness: 1.5×1.5 mm^2 and 1 µm; frame size and thickness: 5.0×5.0 mm^2 and 200 µm; Silson Ltd, Warwickshire, UK), which was previously plasma cleaned using a radiofrequency power of 18 W for 30 s (Harrick Plasma, PDC-32G, Ithaca, New York, USA), is placed in a 3 cm-diameter Petri dish containing 1.7 mL of medium. 300 µL of cell suspension with approximately 3.8×10^5 cells$\cdot mL^{-1}$ are subsequently added. The Petri dish is then placed in the incubator for roughly 30 h to promote cell adhesion and proliferation. The DNA is fluorescently labeled using the Click-iT EdU Alexa Fluor 647 imaging kit (C10340, Thermo Fisher Scientific, Waltham, MA, USA). In this cell proliferation assay, EdU (5-ethynyl-2'-deoxyuridine), a nucleoside analog of thymidine, is incorporated into DNA during DNA synthesis. Following the incubation period, the cells are chemically fixed using 3.7% formaldehyde stabilized with 1% methanol. After the fixation process, the labeling process is completed following the manufacturer's protocol. The cells are then rinsed with, and subsequently stored in, 1× phosphate buffered saline (Sigma-Aldrich) until the vitrification and lyophilization processes are performed, as described elsewhere [19,20]. To prevent rehydration and preserve the integrity of the fluorophore, the samples are stored in a light-protected desiccator until the measurements are performed.

2.2. Experimental setups

All X-ray propagation-based phase contrast holographic-tomography, so-called "holotomography" [21], measurements detailed in this work are performed using the Göttingen Instrument for Nano-Imaging with X-rays (GINIX) [22,23] endstation at the coherence applications beamline P10 at the PETRA III storage ring (DESY, Hamburg, Germany). The beam is delivered by a 5 m-long undulator and is subsequently monochromatized by a Si-111 double-crystal monochromator to an energy $E_{ph} = 8.0$ keV. Entrance slits to the Kirkpatrick-Baez (KB) mirrors are tuned to 0.4×0.4 mm^2. The KB mirrors, oriented in a cross-orthogonal manner, focus the beam to a spot size of 300×350 nm^2 (vertical × horizontal, FWHM). An X-ray waveguide, consisting of lithography-defined channels in silicon [24,25], is positioned in the focus of the KB mirrors. The waveguide acts as a spatial and coherence filter and serves as a quasi point-source ($\leq$ 20 nm) which produces spherical wavefronts. After coupling into the waveguide, the intensity I_0 of the beam is approximately 2.1×10^9 photons$\cdot s^{-1}$. The sample is mounted on a fully motorized sample tower consisting of three translational motors (SLC-1760 and SHL-1D20N-10, SmarAct, Oldenburg, Germany). Behind the sample an on-axis visible-light microscope, operated in reflectivity mode, is used to locate a desired region of the sample. The sample is placed at a series

Biomedical Optics EXPRESS

of defocus positions $z_1 = \{50.8, 51.8, 60.8\}$ mm with respect to the focus position at $z_0 = 0$ mm. The sample-to-detector distance z_2 is approximately 5.02 m. Correspondingly, the magnifications $M = {(z_1 + z_2)}/{z_1}$ and effective pixel sizes $p_{\text{eff}} = {p}/{M}$, where p is the detector pixel size, of each defocus position are $\{99.8, 97.9, 83.6\}$ and $\{65.1, 66.4, 77.8\}$ nm, respectively. Per defocus position the sample is rotated over an angular range of $\theta \in [0°, 180°]$ in 1500 equidistant steps. Thus, 1501 projections are recorded for every defocus position. At the beginning and end of the tomographic recording 50 empty projections (flat fields) are recorded. An empty projection is the recorded intensity when the sample is not in the beam path and is used to characterize the probing wavefront. Furthermore, after the recording, 20 images of the camera dark current are acquired. All projections are recorded by a near-field, scintillator-based fiber-coupled scientific CMOS (sCMOS) detector (Photonic Science, East Sussex, UK; 2048 × 2048 pixels; pixel size: 6.5 × 6.5 μm^2). The exposure time τ for each projection is 1 s. A schematic of the holotomography experimental setup is shown in Fig. 1(a). A reconstructed tomographic slice of a single cell is shown in Fig. 1(b)-c.

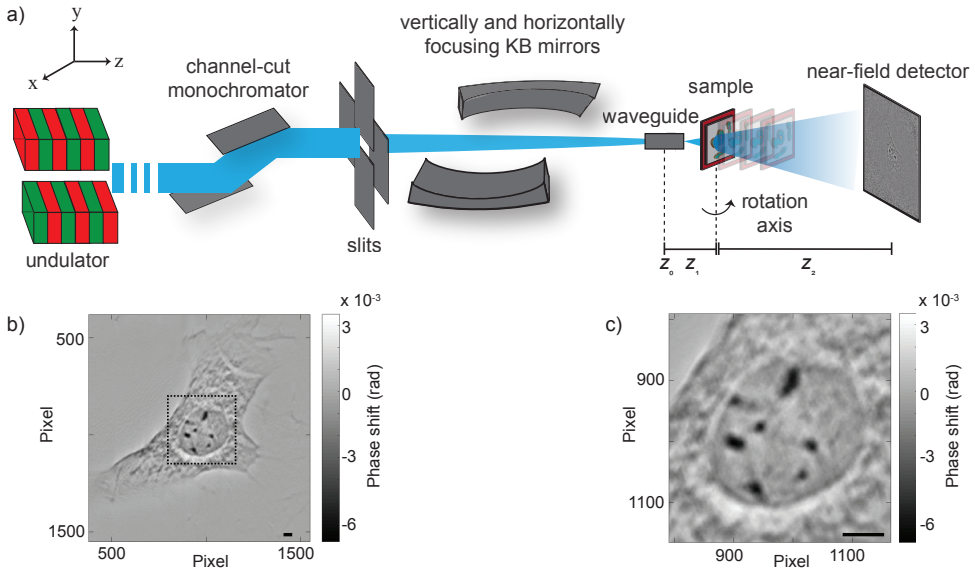

Fig. 1. Schematic of the experimental setup for X-ray propagation-based phase contrast tomography measurements. The X-rays are generated by an undulator and are subsequently monochromatized. The beam is focused by a set of KB mirrors prior to being coupled into the waveguide. The sample is mounted on a fully motorized stage and placed at a series of defocused positions z_1 with respect to the focus position at z_0. Projections are recorded at a sample-to-detector distance of z_2. b) Reconstructed tomographic slice of a cell. The cell nucleus is bound by the dotted square. c) Zoom-in of the bound region from subfigure b). All scale bars are 5 µm.

The radiation dose D, i.e., the energy deposited per unit mass in units of Gy (Gray, J/kg), of the holotomography measurements is estimated using the intensity I_0 and energy E_{ph} of the incident beam, as well as the irradiated area $\Delta_x\Delta_y$ and total exposure time τ_{total}:

$$D = \frac{I_0 \tau_{\text{total}} E_{\text{ph}}}{l \rho_m \Delta_x \Delta_y}. \tag{1}$$

The total exposure time accounts for all angular orientations for all defocus positions and includes, per defocus position, an additional 50 ms to account for the time necessary for the beam shutter

Biomedical Optics EXPRESS

to open and close. The irradiated area is calculated using the effective pixel size of the first defocus position and number of detector pixels N. Thus, $\Delta_x\Delta_y = p_{\text{eff}}^2 \times N = 1.78{\times}10^{-8}\ \text{m}^2$. For calculating the radiation dose on a biological sample with an averaged empirical formula [26] of $H_{50}C_{30}N_9O_{10}S_1$, as is considered here, an attenuation length $l = 7.46{\times}10^{-4}$ m and mass density $\rho_m = 1.35\ \text{g}{\cdot}\text{cm}^{-3}$ are commonly used [27]. Inserting these values into Eq. (1) a radiation dose of $D = 9.0{\times}10^5$ Gy is calculated. This value represents an upper limit. This is because, due to the substrate itself, the sample cannot be irradiated from all angles in a 180° rotation. Thus, angles lying within this "missing wedge" are not contained in the data set. The maximum allowable dose for cells in the hard X-ray regime was studied for a range of different sample environments [28]. For the dose range applied here no structural deterioration is expected in the dehydrated state. In Ref. [29], dose efficiency of holographic imaging in the hard X-ray regime is discussed in detail.

Prior to the X-ray measurements the samples are imaged with a custom-built confocal microscope [17,30] (Abberior Instruments, Göttingen, Germany) equipped with a high numerical aperture (NA) air objective (40×, NA = 0.95, UPLSAPO, Olympus). Here, image acquisition requires an air objective as the 200 µm-thick substrate frame in combination with a glass coverslip exceeds the working distance of water/oil immersion objectives and application of immersion liquid directly on the sample substrate would interfere with the X-ray measurements. The samples are raster scanned with lateral step sizes of $100 \times 100\ \text{nm}^2$ and an axial step size of 250 nm. The excitation wavelength and power are 632 nm and 120 µW, respectively. A dwell time of 0.29 ms is used. We refrain from recording z-stacks using STED microscopy as doing so results in severe photobleaching.

2.3. Data analysis

The phase reconstruction process is performed using the HoloTomoToolbox [31]. Every projection I_{proj} is first corrected using the averaged dark image $\bar{I}_{\text{dark}}$ and averaged empty projection $\bar{I}_{\text{empty}}$ such that $I_{\text{corr}} = \frac{I_{\text{proj}} - \bar{I}_{\text{dark}}}{\bar{I}_{\text{empty}} - \bar{I}_{\text{dark}}}$. The corrected projections are then rescaled to match the magnification of the first defocus position and are subsequently aligned using a sub-pixel image registration algorithm [32] to account for any lateral shifts that may have occurred during the image acquisition process. Following this step the corrected projections are reconstructed using the linear contrast transfer function (CTF) [33]. If necessary, the reconstructed projections are spatially shifted to account for misalignment of the rotation axis. Projections acquired in the missing wedge are excluded from the tomographic reconstruction. For the three presented data sets the average missing wedge is 33°. Tomographic reconstructions are performed using the filtered backprojection function *astraFBP* of the ASTRA toolbox [34,35], yielding access to the phase shift $\phi(\mathbf{r})$ induced by each voxel.

The illuminated volumes of the sample differ for the tomography and confocal measurements. Consequently, the effective pixel size and field of view (FOV) rendered from each modality differ. To account for this circumstance, image registration is performed using self-written MATLAB (The MathWorks, Inc., Natick, MA, USA) scripts, thus enabling the direct correlation of the data sets in a pixel-wise manner. The registration process is based upon the assumption that the cell nucleus is approximately ellipsoidal in shape and contains the most biological material in its center plane as that plane has the largest area. Details about the registration process are found in Fig. S1 in Supplement 1. For all three biological cells, the center plane of each confocal volume is determined by integrating all detected photon counts for each micrograph of the z-stack (Figure S1a). The micrograph with the largest integrated value, and thus largest amount of DNA, is used to define the center plane (Fig. S1b) of the respective confocal volume. The center slice of each reconstructed tomographic volume is determined by first defining a loose region-of-interest (ROI) around the nucleus in a slice for which the nucleus is visually well-defined (Figure S1c,d). The ROI is kept constant for all 2048 reconstructed slices and the reconstructed phase shift values bound by the ROI are integrated for each slice of the tomographic volume (Fig. S1e). The slice

Biomedical Optics EXPRESS

with smallest integrated phase shift value, and thus the most biological material, defines the center slice of the respective tomographic volume (Fig. S1f).

The reconstructed tomograms have a voxel edge length of 65.1 nm, whereas the axial step size used for the confocal acquisition is 250 nm. To enable a direct comparison between the two imaging modalities, 4 reconstructed tomographic slices are added in a pixel-wise manner such that the result represents a 260.4 nm-thick slice of the nucleus (Fig. S1g). Every 260.4 nm-thick slice is subsequently resized in the $x - y$ plane such that it has the same pixel size as the confocal micrographs. This way, we are able to compare and register data stemming from different imaging methods. Here, each method is sensitive to different substructures within the nuclei, thus the superior resolution we obtain by X-ray tomography provides an advantage despite this resampling. For each tomographic volume, 112 slices are used to create 28 slices, i.e., the number of confocal micrographs. The 112 slices used for this rendering process are selected with respect to the center slice, i.e., the 56 slices below and 55 slices above. Indeed, each of the 28 tomographic slices is 10.4 nm thicker than each confocal slice. However, this difference collectively accounts for only 291 nm, or 4%, of the total height of the confocal volume and is disregarded. The 260.4 nm-thick slices are used for subsequent analysis.

The next step is to orient and resize the slices to the angular orientation and FOV of the confocal micrographs. Towards this end, and for each biological cell, a 2D logic mask is manually defined around the nucleus of both center frames (Fig. S1h,i) and their center-of-mass and angular orientation are determined. Note that we here perform the segmentation manually and take great care not to introduce any artifacts at this step. By doing so, we account for the low-contrast and high-background data stemming from the single cells. For future applications of the method with higher throughput, an automation of the segmentation, possibly involving machine learning algorithms, would be highly desirable. Indeed, for tomograms with higher electron density contrast, such as tissue samples, this would likely be successful. The logic mask of the center reconstructed slice is subsequently rotated and translated such that it has the same angular orientation and center-of-mass as the logic mask of the center confocal micrograph. Note that this approach would not work for perfectly spherical cell nuclei, which, however, are highly unlikely to occur. Following this step, each 260.4 nm-thick tomographic slice undergoes identical transformation changes as the logic mask of the center tomographic slice (Fig. S1j). Furthermore, a 3D logic mask is created which renders the region surrounding the nucleus null. The mask is created by manually outlining the nucleus of each confocal micrograph composing the z-stack. The 3D logic mask is applied to both the confocal data and the reconstructed tomogram slices to render unwanted regions, e.g., the cell body, null from subsequent analysis. An example of a masked tomographic slice is shown in Fig. S1k. To verify that the confocal micrographs and tomographic slices represent the same volume of the nucleus, the phase shift or, equivalently, electron density, of each masked slice is integrated (Fig. S1l) and compared to the integrated photon count of the confocal data (Fig. S1a). If necessary, the slices are spatially shifted such that the slice with the smallest integrated phase, or largest electron density, corresponds to the confocal micrograph with the largest integrated photon count.

3. Results and discussion

3.1. DNA distribution in cell nuclei

All measurements presented in this work are performed on lyophilized NIH-3T3 fibroblasts adhered on X-ray transmissive silicon-nitride substrates. In total, three cells are included, for which we obtained complete data sets, i.e., x-ray phase-contrast tomography and confocal imaging. While the current "gold standard" is certainly cryo-preservation of cellular samples before and during X-ray imaging, here we follow a different route, which focuses on methods development towards the investigation of living cells in close-to-physiological environments. We are aware that the investigation of lyophilized samples represents an intermediate step towards – in the future –

Biomedical Optics EXPRESS

the study of fixed-hydrated and eventually living cells. Although in general the lyophilization process may alter nanostructures, the integrity of mammalian DNA remains intact during the process [36]. Visible-light micrographs of all three biological cells in the lyophilized state are shown in Fig. S2 in Supplement 1. For confocal z-stack measurements, the sample is mounted on a fully motorized stage and subsequently raster scanned. We fluorescently label the incorporated nucleoside analog of thymidine. Thus, the recorded signal is, in first approximation, proportional to the amount of DNA distributed throughout the nucleus. An example of a confocal z-stack of a cell nucleus in interphase is shown in Fig. 2(a). This nucleus is shown throughout Figs. 2–6 and is hereinafter referred to as "nucleus 1".

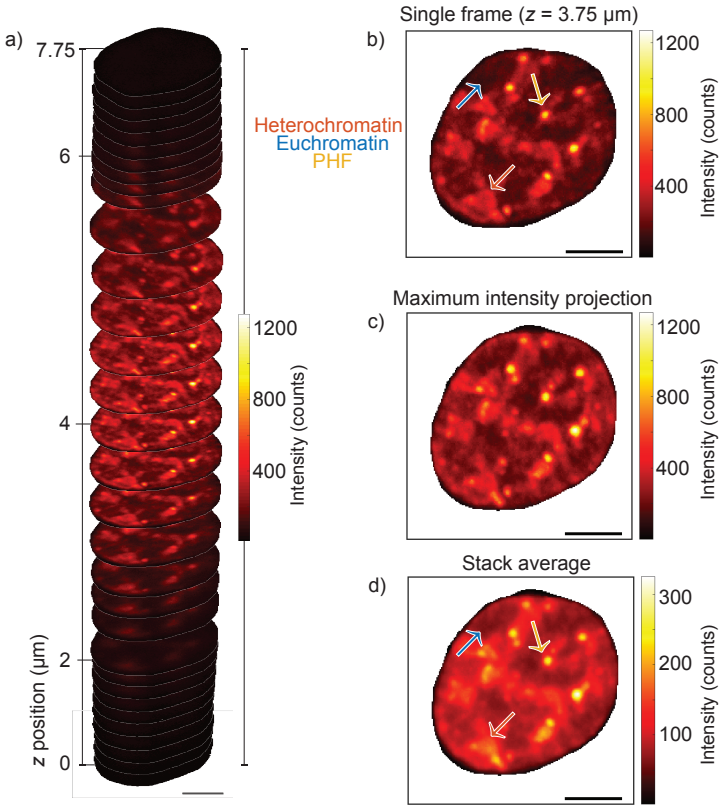

Fig. 2. a) Confocal z-stack of a lyophilized, whole cell nucleus. All individual micrographs composing the stack have the same colorscale. b) A single micrograph from the confocal stack shown in a). A PHF is indicated by the yellow arrow, and examples of the surrounding heterochromatin and euchromatin are indicated by the orange and blue arrows, respectively. c) The maximum intensity projection of the stack shown in a). d) The average projection of the stack shown in a). Note that the color scale of the average projection differs from those of a)-c). All scale bars are 5 μm.

In Fig. 2 three distinct regions are observed: i) high-intensity globular regions, ii) the surrounding medium-intensity regions and iii) low-intensity regions. These regions are more-easily identifiable when inspecting a single image of the z-stack, as shown in Fig. 2(b), and are also visible in the maximum intensity projection (Fig. 2(c)) and stack average (Fig. 2(d)). The entire confocal stack is considered when rendering the maximum intensity projection and stack average.

Biomedical Optics EXPRESS

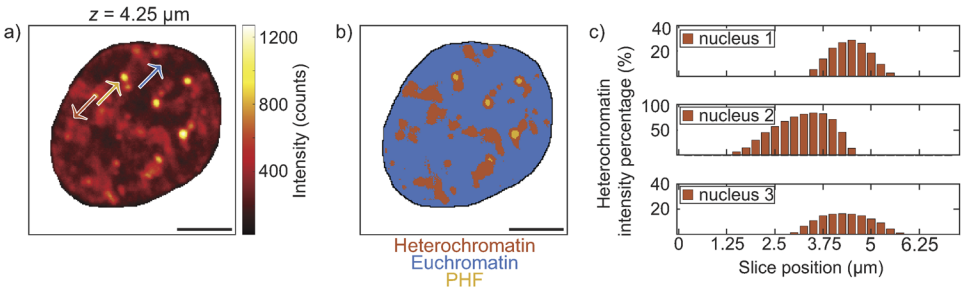

Fig. 3. a) The center confocal micrograph of nucleus 1. The yellow arrow indicates the location of a PHF. Examples of heterochromatin and euchromatin are indicated by the orange and blue arrows, respectively. b) Logic mask corresponding to the confocal micrograph shown in subfigure a). The spatial distributions of euchromatin, heterochromatin and PHFs are shown in blue, orange and yellow, respectively. For each micrograph of the confocal stack a unique logic mask is created using the same threshold values used to create subfigure b). c) For every micrograph of the confocal stack the percentage of intensity stemming from heterochromatin is calculated. All scale bars are 5 µm.

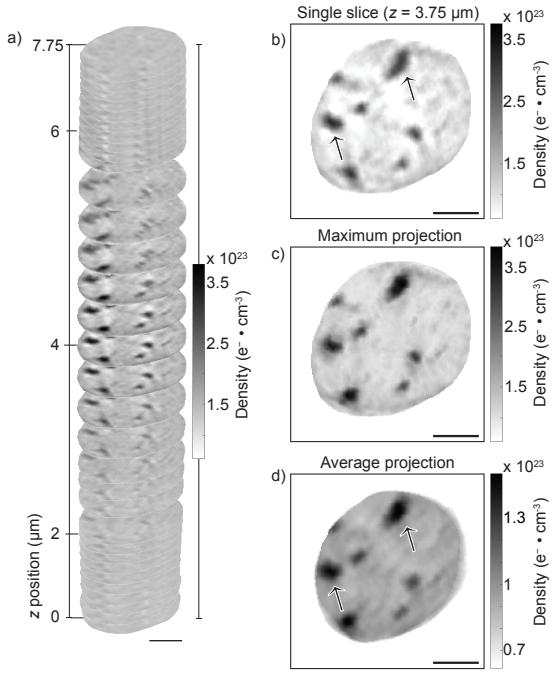

Fig. 4. Electron density of the lyophilized nucleus shown throughout Fig. 2. a) Stack of reconstructed tomogram slices each with a voxel size of $100 \times 100 \times 260.4$ nm^3. b) A single slice from the reconstructed tomogram show in a). Examples of nucleoli are indicated by black arrows. This slice corresponds to the same plane as shown in Fig. 2(b). c) The maximum projection of the stack show in subfigure a). d) The average projection of the stack shown in subfigure a). Note that the color scale of the average projection differs from those of a)-c). All scale bars are 5 µm.

Biomedical Optics EXPRESS

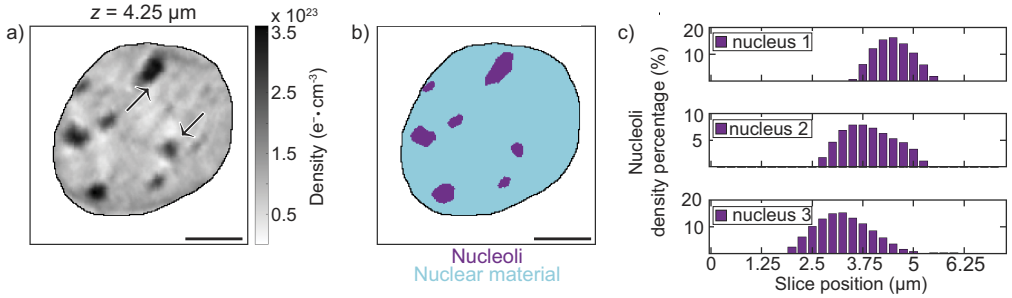

Fig. 5. a) The center tomographic slice of nucleus 1. Note that this is the same plane as shown in Fig. 3(a). Examples of nucleoli are indicated by the black arrows. b) Logic mask corresponding to the reconstructed slice shown in a). The spatial distribution of nucleoli and the surrounding nuclear material are shown in purple and cyan, respectively. For every slice of the tomographic stack a unique logic mask is created using the same threshold used to segment subfigure a). Subfigures a), b), are also shown in Fig. S3f) and h), respectively, in Supplement 1. c) For every tomographic slice the percentage of its total electron density stemming from nucleoli is calculated. All scale bars are 5 µm.

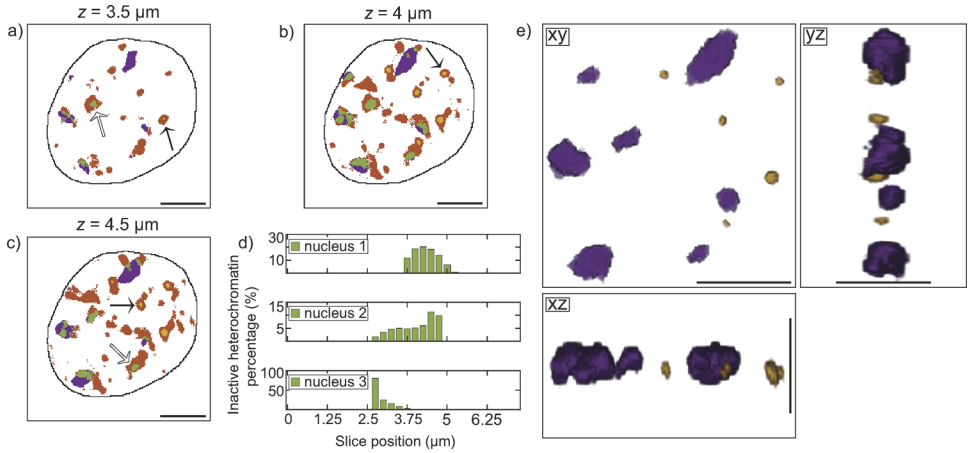

Fig. 6. a)-c) Three examples (slices) of logic masks for nucleus 1 showing the spatial distribution of nucleoli (purple), heterochromatin (orange), PHFs (yellow) and inactive heterochromatin (green). Euchromatin occupies all regions not occupied by heterochromatin, PHFs or nucleoli and is shown in white. White arrows indicate regions where inactive heterochromatin is completely surrounded by heterochromatin. Black arrows indicate regions where PHFs are completely surrounded by heterochromatin. d) For every slice the percentage of heterochromatin that is inactive is calculated. e) 3D visualization of the nucleoli and PHFs belonging to nucleus 1 (voxel size: $100 \times 100 \times 260.4$ nm^3). All scale bars are 5 µm

Biomedical Optics EXPRESS

Within the nucleus of a eukaryotic cell, 2 nm-thick DNA double helices [1] are wrapped around octamers of histones, which subsequently form 10 nm-diameter nucleosomes [37]. Nucleosomes spaced along the genome form a nucleofilament known as chromatin. Chromatin is broadly categorized into two classes: heterochromatin and euchromatin. Euchromatin is known to be gene-rich, involved in active processes such as transcription and is de-condensed during interphase [38]. Heterochromatin remains condensed throughout the cell cycle [39], is necessary for the inhibition of the expression of euchromatin genes [40] and tends to be more adenine−thymine (AT)-rich when compared to euchromatin [41]. The amount of thymine, and thus fluorescent label, is nevertheless a good measure for the amount of DNA present [42]. From comparing our data to fluorescence recovery after photobleaching experiments and differential interference contrast micrographs [41,42], we interpret the medium-intensity and low-intensity regions observed throughout Fig. 2 to be heterochromatin and euchromatin, respectively.

A sub-class of heterochromatin is PHFs [43]. PHFs are AT-rich regions of heterochromatin and surround chromosome structures such as centromeres [39]. PHFs contain the histone protein H3 [44] and have been implicated in the gene silencing that occurs by chromosome rearrangement or transposition [45,46]. PHFs have been fluorescently imaged in mouse cells [42,44] and are easily identifiable due to their globular shape and intense staining by 4′, 6−diamidino−2−phenylindole (DAPI). DAPI binds strongly to AT-rich sequences of DNA via groove binding and intercalation [47,48]. This makes DAPI staining comparable to the Click-iT EdU label, a nucleoside analog of thymidine, which we employ in our work. PHFs have a diameter of roughly 1 µm [42], which corresponds well to the size of the high-intensity regions observed throughout Fig. 2. Therefore, and from further comparison to fluorescence in situ hybridization micrographs [44,49], we interpret these high-intensity globular regions as PHFs. Subsequent analysis presented in this work is based on the segmentation of PHFs, heterochromatin and euchromatin.

Details of the segmentation process are shown in Fig. S3 in Supplement 1: Using the center confocal micrograph (Fig. 3(a), Fig. S3a), we introduce an intensity-value threshold which, through visual inspection, segments PHFs (Figure S3b). When segmenting PHFs we use the largest threshold possible that does not result in the inclusion of heterochromatin structures. Next, and again using the center confocal micrograph, we segment heterochromatin (Fig. S3c) and euchromatin (Fig. S3d) by introducing a 2.0-fold intensity threshold of the fluorescence signal: we determine an intensity value threshold such that the mean intensity of pixel values above the threshold is 2.0-fold larger than the mean intensity of pixels with intensity values below the threshold, thus segmenting the heterochromatin and euchromatin regions. This 2.0-fold criterion is based on previous work [42] whose authors used DAPI to label DNA within NIH-3T3 fibroblasts and found the intensity of heterochromatin to be 2.0 ± 0.3-fold higher than the intensity of euchromatin. For each micrograph of the z-stack the heterochromatin, euchromatin and PHFs are segmented using the same two thresholds used to segment the center micrograph. For each micrograph a logic mask is created which maps the spatial distribution of each substructure. This analysis is separately performed for the remaining two biological cells. The center confocal micrograph of nucleus 1 and its corresponding logic mask are shown in Fig. 3(a) and (b), respectively. These two figures are also shown in Fig. S3a and e, respectively.

For all confocal micrographs composing the z-stack, we calculate the percentage of their overall intensity due to heterochromatin, as shown in Fig. 3(c). The mean percentage values for nuclei 1, 2 and 3 are 14%, 45% and 9%, respectively. A plausible explanation for the increase in percentage, and thus heterochromatin, for nucleus 2 is that it might be in the S-phase (synthesis phase of the eukaryotic division cycle) of the cell-cycle [50], whereas nuclei 1 and 3 would be in the earlier G1 phase (gap/growth 1 phase). Furthermore, for each biological cell, we calculate the heterochromatin volume fraction bound by the first and last micrographs which contain heterochromatin: for each confocal micrograph both the number of pixels defined by heterochromatin and the number of pixels defined by the nucleus area are summed. The ratio

Biomedical Optics EXPRESS

of the two numbers for the total, i.e., the bound, volume defines the heterochromatin volume fraction. Nuclei 1 and 3 have heterochromatin volume fractions of approximately 8% and 5%, respectively, and nucleus 2 has a volume fraction of approximately 34%. This increase in heterochromatin volume for nucleus 2 supports our interpretation that it might be in the S-phase. The mean heterochromatin intensities of all three biological cells are found to be comparable to each other. For each cell, the mean heterochromatin intensity is 2.5-fold higher than the mean euchromatin intensity. The values are calculated by taking the ratio of the average results of all three biological cells. The 2.5-fold higher intensity of heterochromatin indicates the intensity distribution of heterochromatin and euchromatin differs as a function of z-slice, thus the slight deviation from the ratio of 2.0, which we applied to the center slice for determination of the threshold value. Similarly, we find that the mean PHFs intensity of all three cells is comparable and is approximately 3.0-fold higher than the mean intensity of all other DNA.

3.2. Quantitative X-ray tomography of cell nuclei

From the discussion above it becomes clear that our confocal microscopy measurements provide information about the spatial distribution and intensity of euchromatin, heterochromatin and PHFs. However, DNA exists in other structures within the cell nucleus which are not easily identifiable in our confocal data, such as nucleoli. These subnuclear bodies play a role in many functions including ribosomal RNA (rRNA) synthesis, DNA repair and replication, and ribosomal DNA (rDNA) transcription [51,52]. The morphology and size of nucleoli are linked to transcription activity and are thus dependent on the cell cycle [53]. Indeed, nucleoli regulate the cell cycle and disassemble and reassemble at the beginning and end of mitosis, respectively [54,55].

Here, to spatially segment the nucleoli and to quantify their electron density, we complement confocal microscopy with holotomography, a 3D full-field imaging technique sensitive to the electron density of matter. In the holotomography experimental setup, shown schematically in Fig. 1(a), the KB-focused X-rays are coupled into a waveguide which acts as a quasi point source emitting a highly divergent and coherent spherical wavefront which is ideally suited for near-field imaging. The sample is placed at a series of defocus position z_1, and at each defocus position it is rotated over an angular range in equidistant steps. At every angular step, a holographic projection is recorded at a sample-to-detector distance z_2. Projections are recorded at multiple distances to account for the zero-crossings of the CTF produced when imaging weakly absorbing objects with a slowly varying phase, e.g., a biological cell [33]. The holographic projections encode the projected phase shift or, equivalently, the projected electron density distribution of the sample.

The phase reconstruction is performed by processing all acquired holographic projections via the linear CTF algorithm. In first approximation, we assume the sample's elemental composition – but not its density – is homogeneous. The CTF algorithm is implemented in such a way that the maximum reconstructed phase of any pixel cannot be greater than zero radians. The resulting 2D reconstructed phase maps are subsequently used to reconstruct the 3D volume by the inverse Radon transform. One consequence of the inverse Radon transform is that a voxel may have a positive phase shift value, thus leading to a negative electron density value. To account for this circumstance, all phase shift values are offset by the same constant value such that all tomographic voxels have negative values. Towards this end, an ROI is defined which is used for background correction (Fig. S1f, black box). For each tomographic slice the mean phase shift value of the background region is calculated. The maximum background value is determined and subsequently subtracted from each tomographic slice, thus offsetting them. Following this step, the electron density of the sample is quantified. The phase shift $\phi(\mathbf{r})$ is related to the local electron density $\rho_e(\mathbf{r})$ of each voxel by:

$$\rho_e(\mathbf{r}) = \frac{-\phi(\mathbf{r})}{\nu\lambda r_0}, \tag{2}$$

Biomedical Optics EXPRESS

where v, λ and r_0 represent the voxel side length, X-ray wavelength and classical electron radius, respectively. Note that the electron density is quantified using the background corrected, non-resized tomographic slices with $v = 65.1$ nm.

To correlate the tomography and confocal volumes in a pixel-wise manner, all tomographic slices and confocal micrographs must have the same pixel size and FOV. To ensure this, we register all tomographic slices to the confocal micrographs, thus rendering them suitable for direct comparison. An example of a stack of registered slices, expressed in terms of the local electron density, is shown in Fig. 4(a).

As can been seen throughout Fig. 4(a) there exist globular regions about 2 µm in size with high electron densities. These regions are more easily identifiable when viewing a single slice from the stack, as shown in Fig. 4(b). Examples of the dense, globular regions are indicated by black arrows. These regions are also visible in the maximum projection (Fig. 4(c)) and stack average (Fig. 4(d)). The entire 28-slice tomographic stack is considered when rendering the maximum projection and stack average. The diameter of a nucleolus is roughly 2 µm [56], which corresponds well to the dense, globular regions observed throughout Fig. 4. Thus, by visual inspection and further comparison to visible light micrographs, where such structures are clearly visible [56,57], we interpret these regions as nucleoli. Subsequent analysis is based on the segmentation of nucleoli.

Using the center tomographic slice, as shown in Fig. 5(a), an intensity-value threshold is determined which, through visual inspection, spatially segments the nucleoli (Fig. 5(b)). This threshold is kept constant and is applied to each slice of the tomographic stack. For each slice, a logic mask is created which maps the spatial distribution of the nucleoli. For each of the three biological cells we determine the mean electron density of all segmented nucleoli and find that their values are comparable to each other. We find the mean electron density of nucleoli to be approximately 2.3-fold larger than the mean nucleus electron density. This increase is on the same order as in other work, whose authors found the average electron density of a mouse A9 cell nucleolus to be approximately 1.5-fold larger than the average nucleus density [16]. Furthermore, for each slice of a tomographic stack, we calculate the percentage of its electron density stemming from the nucleoli, as shown in Fig. 5(c). The mean percentage values for nucleus 1, 2 and 3 are 9%, 4% and 6%, respectively, thus, on the same order of magnitude.

3.3. *Complementary information from visible light fluorescence and X-ray tomography of cell nuclei*

So far, we have discussed the results of the X-ray propagation-based phase contrast tomography data independently from the confocal data. However, a benefit of acquiring data using both imaging modalities on the same sample is that the data can be combined and correlated. Towards this end, we first create a logic mask for each frame which maps the spatial distribution of heterochromatin (orange), PHFs (yellow), nucleoli (purple) and heterochromatin colocalized within nucleoli (green), as shown in Fig. 6(a)-c. We observe heterochromatin to be distributed throughout the nucleus area and near its periphery. Similar distributions are visible in electron micrographs [58,59]. In addition, we observe heterochromatin to completely surround PHFs, as indicated by the black arrows throughout Fig. 6(a)-c. Nucleoli are hubs for the organization of inactive heterochromatin, i.e., heterochromatin with low gene density [60]. We thus interpret the heterochromatin that we observe colocalized within nucleoli (Fig. 6(a)-c, green) inactive. For each frame we calculate the percentage of heterochromatin that is inactive, as shown in Fig. 6(d). The mean percentage values for nucleus 1, 2 and 3 are 11%, 6% and 13%, respectively. A compilation of the distributions of quantified attributes, i.e., Fig. 3(c), Fig. 5(c) and Fig. 6(d), is shown in Fig. S4. Within the nucleus, euchromatin occupies all regions that are not occupied by heterochromatin, PHFs or nucleoli and is shown in white in Fig. 6(a)-c; we observe that euchromatin is, in some instances, also found in the vicinity of the nucleoli.

Biomedical Optics EXPRESS

From the confocal data we find the mean heterochromatin intensity of all three nuclei to be comparable and 2.5-fold larger than the mean euchromatin intensity. When comparing the mean electron density of heterochromatin of all three nuclei we find their values to be comparable and 1.1-fold larger than the mean euchromatin electron density. Thus, heterochromatin has nearly the same electron density as euchromatin, suggesting that the two classes of chromatin have comparable amounts of non-nucleosomal materials such as proteins. Previous work [41], similar to our results, found the electron density of heterochromatin in live NIH-3T3 cells to be approximately 1.5-fold larger than euchromatin. When considering all three nuclei, we find the mean nucleoli electron density to be approximately 2.1-fold larger than the mean PHF electron density. Additionally, when considering all three nuclei, we find the mean nucleoli volume to be approximately 40-fold larger than the mean PHF volume.

To visualize nucleoli and PHFs in 3D we use the software Avizo Lite 9 (Thermo Fisher Scientific, Waltham, MA, USA). The 3D segmentation of nucleoli and PHFs of nucleus 1 is shown in Fig. 6(e). As can be seen throughout the $x-z$ and $y-z$ planes, all structures appear to be restricted to a single plane which is parallel to the sample substrate. Similar observations are made for nucleus 2 and 3. This "line-up" may be an artifact of having the cells adhered to a flat surface. We find the nucleoli to be approximately ellipsoidal in shape and the PHFs, which have been mathematically modeled [61], to be approximately spherical in shape.

4. Summary and conclusions

To summarize, we exploit the combination of X-rays and visible light fluorescence to image whole, intact cell nuclei in 3D. In particular, we correlate X-ray propagation-based phase contrast tomography with confocal microscopy. This combined approach allows us to spatially segment and quantify the electron density and fluorescence intensity of substructures located within a complex biological system. Analysis of the confocal micrographs, which gives rise to the amount of DNA present in the nucleus, reveals regions of euchromatin, heterochromatin and PHFs. By contrast, X-ray propagation-based phase contrast tomography, a technique sensitive to the electron density of matter, reveals dense, globular regions corresponding to nucleoli. We find that nucleoli are the densest structures in the nucleus and have approximately twice the mean electron density as PHFs due to the high protein concentration. We also find the volume of nucleoli to be an order of magnitude larger than the volume of PHFs. While the mean electron density of heterochromatin and euchromatin are nearly identical, heterochromatin contains more than twice the amount of DNA, as revealed by confocal microscopy. This study highlights the importance of combining and correlating different imaging modalities, specifically X-ray propagation-based phase contrast tomography and confocal microscopy. Our approach can be applied to a variety of complex biological systems such as biological cells or tissues and enables substructures including intracellular organelles that can be fluorescently labeled to be segmented and quantitatively characterized in a spatially-resolvable manner. Moreover, in future experiments, with even higher resolution, substructures within the nuclear regions may be resolved.

Funding. Bundesministerium für Bildung und Forschung (05K19MG3); Deutsche Forschungsgemeinschaft (EXC 2067/1-390729940, SFB 860/B10).

Acknowledgments. The authors thank M. Eckermann, M. Reichardt, G. Brehm, P. Luley and M. Sprung for fruitful discussions and technical assistance during the beam time, as well as for setting up the beam at the P10 coherence applications beamline. We also thank J. Herbst for providing technical assistance with sample preparation. We acknowledge support by the Open Access Publication Funds of the Göttingen University.

Disclosures. The authors declare no conflicts of interest.

Data availability. Data underlying the results presented in this paper are not publicly available at this time but may be obtained from the authors upon reasonable request.

Supplemental document. See Supplement 1 for supporting content.

Biomedical Optics EXPRESS

References

1. J. Watson and F. Crick, "Molecular structure of nucleic acids," Nature **171**(4356), 737–738 (1953).
2. K. Maeshima, S. Hihara, and M. Eltsov, "Chromatin structure: Does the 30-nm fibre exist in vivo?" Curr. Opin. Cell Biol. **22**(3), 291–297 (2010).
3. J. Kirz, C. Jacobsen, and M. Howells, "Soft x-ray microscopes and their biological applications," Q. Rev. Biophys. **28**(1), 33–130 (1995).
4. S. Sahl, S. Hell, and S. Jakobs, "Fluorescence nanoscopy in cell biology," Nat. Rev. Mol. Cell Biol. **18**(11), 685–701 (2017).
5. E. Pereiro, "Correlative cryo-soft x-ray tomography of cells," Biophys. Rev. **11**(4), 529–530 (2019).
6. G. Schneider, P. Guttmann, S. Heim, S. Rehbein, F. Mueller, K. Nagashima, J. B. Heymann, W. G. Müller, and J. McNally, "Three-dimensional cellular ultrastructure resolved by x-ray microscopy," Nat. Methods **7**(12), 985–987 (2010).
7. W. G. Müller, J. B. Heymann, K. Nagashima, P. Guttmann, S. Werner, S. Rehbein, G. Schneider, and J. McNally, "Towards an atlas of mammalian cell ultrastructure by cryo soft x-ray tomography," J. Struct. Biol. **177**(2), 179–192 (2012).
8. R. Eils, S. Dietzel, E. Bertin, E. Schröck, M. R. Speicher, T. Ried, M. Robert-Nicoud, C. Cremer, and T. Cremer, "Three-dimensional reconstruction of painted human interphase chromosomes: Active and inactive x chromosome territories have similar volumes but differ in shape and surface structure," J. Cell Biol. **135**(6), 1427–1440 (1996).
9. E. Smith, G. McDermott, M. Do, K. Leung, B. Panning, M. Le Gros, and C. Larabell, "Quantitatively imaging chromosomes by correlated cryo-fluorescence and soft x-ray tomographies," Biophys. J. **107**(8), 1988–1996 (2014).
10. R. Kornberg, "Chromatin structure: A repeating unit of histones and dna," Science **184**(4139), 868–871 (1974).
11. H. Jiang, C. Song, C. Chen, R. Xu, K. Raines, B. Fahimian, C. Lu, T. Lee, A. Nakashima, J. Urano, T. Ishikawa, F. Tamanoi, and J. Miao, "Quantitative 3d imaging of whole, unstained cells by using x-ray diffraction microscopy," Proc. Natl. Acad. Sci. U. S. A. **107**(25), 11234–11239 (2010).
12. M. Bartels, M. Priebe, R. Wilke, S. Krüger, K. Giewekemeyer, S. Kalbfleisch, C. Olendrowitz, M. Sprung, and T. Salditt, "Low-dose three-dimensional hard x-ray imaging of bacterial cells," Opt. Nanoscopy **1**(1), 10 (2012).
13. R. Wilke, M. Priebe, M. Bartels, K. Giewekemeyer, A. Diaz, P. Karvinen, and T. Salditt, "Hard x-ray imaging of bacterial cells: Nano-diffraction and ptychographic reconstruction," Opt. Express **20**(17), 19232–19254 (2012).
14. A. Diaz, B. Malkova, M. Holler, M. Guizar-Sicairos, E. Lima, V. Panneels, G. Pigino, A. Bittermann, L. Wettstein, T. Tomizaki, R. Wepf, and A. Menzel, "Three-dimensional mass density mapping of cellular ultrastructure by ptychographic x-ray nanotomography," J. Struct. Biol. **192**(3), 461–469 (2015).
15. C. Gramaccioni, Y. Yang, A. Pacureanu, N. Vigano, A. Procopio, P. Valenti, L. Rosa, F. Berlutti, S. Bohic, and P. Cloetens, "Cryo-nanoimaging of single human macrophage cells: 3d structural and chemical quantification," Anal. Chem. **92**(7), 4814–4819 (2020).
16. C. Song, M. Takagi, J. Park, R. Xu, M. Gallagher-Jones, N. Imamoto, and T. Ishikawa, "Analytic 3d imaging of mammalian nucleus at nanoscale using coherent x-rays and optical fluorescence microscopy," Biophys. J. **107**(5), 1074–1081 (2014).
17. M. Bernhardt, J. D. Nicolas, M. Osterhoff, H. Mittelstädt, M. Reuss, B. Harke, A. Wittmeier, M. Sprung, S. Köster, and T. Salditt, "Correlative microscopy approach for biology using x-ray holography, x-ray scanning diffraction and sted microscopy," Nat. Commun. **9**(1), 3641 (2018).
18. G. Todaro and H. Green, "Quantitative studies of the growth of mouse embryo cells in culture and their development into established lines," J. Cell Biol. **17**(2), 299–313 (1963).
19. B. Weinhausen, J. Nolting, C. Olendrowitz, J. Langfahl-Klabes, M. Reynolds, T. Salditt, and S. Köster, "X-ray nano-diffraction on cytoskeletal networks," New J. Phys. **14**(8), 085013 (2012).
20. V. Piazza, B. Weinhausen, A. Diaz, C. Dammann, C. Maurer, M. Reynolds, M. Burghammer, and S. Köster, "Revealing the structure of stereociliary actin by x-ray nanoimaging," ACS Nano **8**(12), 12228–12237 (2014).
21. P. Cloetens, W. Ludwig, J. Baruchel, D. Van-Dyck, J. Van-Landuyt, J. Guigay, and M. Schlenker, "Holotomography: Quantitative phase tomography with micrometer resolution using hard synchrotron radiation x-rays," Appl. Phys. Lett. **75**(19), 2912–2914 (1999).
22. S. Kalbfleisch, H. Neubauer, S. Krüger, M. Bartels, M. Osterhoff, D. Mai, K. Giewekemeyer, B. Hartmann, M. Sprung, and T. Salditt, "The göttingen holography endstation of beamline p10 at petra iii/desy," AIP Conf. Proc. **1365**, 96–99 (2011).
23. T. Salditt, M. Osterhoff, M. Krenkel, R. Wilke, M. Priebe, M. Bartels, S. Kalbfleisch, and M. Sprung, "Compound focusing mirror and x-ray waveguide optics for coherent imaging and nanodiffraction," J. Synchrotron Radiat. **22**(4), 867–878 (2015).
24. H. Chen, S. Hoffmann, and T. Salditt, "X-ray beam compression by tapered waveguides," Appl. Phys. Lett. **106**(19), 194105 (2015).
25. S. Hoffmann-Urlaub, P. Höhne, M. Kanbach, and T. Salditt, "Advances in fabrication of x-ray waveguides," Microelectron. Eng. **164**, 135–138 (2016).
26. M. Howells, T. Beetz, H. Chapman, C. Cui, J. Holton, C. Jacobsen, J. Kirz, E. Lima, S. Marchesini, and H. Miao, "An assessment of the resolution limitation due to radiation damage in x-ray diffraction microscopy," J. Electron Spectrosc. Relat. Phenom. **170**(1-3), 4–12 (2009).

Biomedical Optics EXPRESS

27. B. Henke, E. Gullikson, and J. Davis, "X-ray interactions: Photoabsorption, scattering, transmission, and reflection at e= 50-30, 000 ev, z= 1-92," At. Data Nucl. Data Tables **54**(2), 181–342 (1993).
28. J.-D. Nicolas, S. Aeffner, and T. Salditt, "Radiation damage studies in cardiac muscle cells and tissue using microfocused x-ray beams: experiment and simulation," J. Synchrotron Radiat. **26**(4), 980–990 (2019).
29. J. Hagemann and T. Salditt, "The fluence–resolution relationship in holographic and coherent diffractive imaging," J. Appl. Crystallogr. **50**(2), 531–538 (2017).
30. M. Bernhardt, J. D. Nicolas, M. Osterhoff, H. Mittelstädt, M. Reuss, B. Harke, A. Wittmeier, M. Sprung, S. Köster, and T. Salditt, "A beamline-compatible sted microscope for combined visible-light and x-ray studies of biological matter," J. Synchrotron Radiat. **26**(4), 1144–1151 (2019).
31. L. Lohse, A. Robisch, M. Töpperwien, S. Maretzke, M. Krenkel, J. Hagemann, and T. Salditt, "A phase-retrieval toolbox for x-ray holography and tomography," J. Synchrotron Radiat. **27**(3), 852–859 (2020).
32. M. Guizar-Sicairos, S. Thurman, and J. Fienup, "Efficient subpixel image registration algorithms," Opt. Lett. **33**(2), 156–158 (2008).
33. S. Zabler, P. Cloetens, J. Guigay, J. Baruchel, and M. Schlenker, "Optimization of phase contrast imaging using hard x-rays," Rev. Sci. Instrum. **76**(7), 073705 (2005).
34. W. Palenstijn, K. Batenburg, and J. Sijbers, "The astra tomography toolbox," in *13th International Conference on Computational and Mathematical Methods in Science and Engineering*, vol. 2013 (2013), pp. 1139–1145.
35. W. Van Aarle, W. Palenstijn, J. Cant, E. Janssens, F. Bleichrodt, A. Dabravolski, J. De Beenhouwer, K. Batenburg, and J. Sijbers, "Fast and flexible x-ray tomography using the astra toolbox," Opt. Express **24**(22), 25129–25147 (2016).
36. M. Zhang, H. Oldenhof, B. Sydykov, J. Bigalk, H. Sieme, and W. Wolkers, "Freeze-drying of mammalian cells using trehalose: Preservation of dna integrity," Sci. Rep. **7**(1), 1–10 (2017).
37. A. Olins and D. Olins, "Spheroid Chromatin Units (v Bodies)," Science **183**(4122), 330–332 (1974).
38. S. Kwon and J. Workman, "The changing faces of hp1: From heterochromatin formation and gene silencing to euchromatic gene expression: Hp1 acts as a positive regulator of transcription," BioEssays **33**(4), 280–289 (2011).
39. C. Maison and G. Almouzni, "Hp1 and the dynamics of heterochromatin maintenance," Nat. Rev. Mol. Cell Biol. **5**(4), 296–305 (2004).
40. K. Weiler and B. Wakimoto, "Heterochromatin and gene expression in drosophila," Annu. Rev. Genet. **29**(1), 577–605 (1995).
41. R. Imai, T. Nozaki, T. Tani, K. Kaizu, K. Hibino, S. Ide, S. Tamura, K. Takahashi, M. Shribak, and K. Maeshima, "Density imaging of heterochromatin in live cells using orientation-independent-dic microscopy," Mol. Biol. Cell **28**(23), 3349–3359 (2017).
42. K. Müller, F. Erdel, M. Caudron-Herger, C. Marth, B. Fodor, M. Richter, M. Scaranaro, J. Beaudouin, M. Wachsmuth, and K. Rippe, "Multiscale analysis of dynamics and interactions of heterochromatin protein 1 by fluorescence fluctuation microscopy," Biophys. J. **97**(11), 2876–2885 (2009).
43. M. Guenatri, D. Bailly, C. Maison, and G. Almouzni, "Mouse centric and pericentric satellite repeats form distinct functional heterochromatin," J. Cell Biol. **166**(4), 493–505 (2004).
44. A. Probst and G. Almouzni, "Heterochromatin establishment in the context of genome-wide epigenetic reprogramming," Trends Genet. **27**(5), 177–185 (2011).
45. C. Francastel, M. Walters, M. Groudine, and D. Martin, "A functional enhancer suppresses silencing of a transgene and prevents its localization close to centromeric heterochromatin," Cell **99**(3), 259–269 (1999).
46. K. Brown, J. Baxter, D. Graf, M. Merkenschlager, and A. Fisher, "Dynamic repositioning of genes in the nucleus of lymphocytes preparing for cell division," Mol. Cell **3**(2), 207–217 (1999).
47. F. Tanious, J. Veal, H. Buczak, L. Ratmeyer, and W. Wilson, "DAPI (4′,6-diamidino-2-phenylindole) binds differently to DNA and RNA: minor-groove binding at AT sites and intercalation at AU sites," Biochemistry **31**(12), 3103–3112 (1992).
48. J. Kapuscinski, "Dapi: A dna-specific fluorescent probe," Biotech. Histochem. **70**(5), 220–233 (1995).
49. K. Salmina, A. Huna, I. Inashkina, A. Belyayev, J. Krigerts, L. Pastova, A. Vazquez-Martin, and J. Erenpreisa, "Nucleolar aggresomes mediate release of pericentric heterochromatin and nuclear destruction of genotoxically treated cancer cells," Nucleus **8**(2), 205–221 (2017).
50. A. Kloc and R. Martienssen, "RNAi, heterochromatin and the cell cycle," Trends Genet. **24**(10), 511–517 (2008).
51. D. Brown and J. Gurdon, "Absence of ribosomal rna synthesis in the anucleolate mutant of xenopus laevis," Proc. Natl. Acad. Sci. U. S. A. **51**(1), 139–146 (1964).
52. F. Boisvert, S. van Koningsbruggen, J. Navascués, and A. Lamond, "The multifunctional nucleolus," Nat. Rev. Mol. Cell Biol. **8**(7), 574–585 (2007).
53. C. Bersaglieri and R. Santoro, "Genome organization in and around the nucleolus," Cells **8**(6), 579 (2019).
54. V. Sirri, S. Urcuqui-Inchima, P. Roussel, and D. Hernandez-Verdun, "Nucleolus: The fascinating nuclear body," Histochem. Cell Biol. **129**(1), 13–31 (2008).
55. P. Roussel, C. André, L. Comai, and D. Hernandez-Verdun, "The rdna transcription machinery is assembled during mitosis in active nors and absent in inactive nors," J. Cell Biol. **133**(2), 235–246 (1996).
56. J. Andersen, C. Lyon, A. Fox, A. Leung, Y. Lam, H. Steen, M. Mann, and A. Lamond, "Directed proteomic analysis of the human nucleolus," Curr. Biol. **12**(1), 1–11 (2002).
57. D. Hernandez-Verdun, P. Roussel, M. Thiry, V. Sirri, and D. Lafontaine, "The nucleolus: Structure-function relationship in rna metabolism," Wiley Interdiscip. Rev. RNA. **1**(3), 415–431 (2010).

Biomedical Optics EXPRESS

58. L. Gurley, R. Walters, S. Barham, and L. Deaven, "Heterochromatin and histone phosphorylation," Exp. Cell Res. **111**(2), 373–383 (1978).
59. W. Nagl, "Heterochromatin elimination in the orchid dendrobium," Protoplasma **118**(3), 234–237 (1983).
60. C. Guetg and R. Santoro, "Formation of nuclear heterochromatin: the nucleolar point of view," Epigenetics **7**(8), 811–814 (2012).
61. S. Eck, S. Wörz, K. Müller-Ott, M. Hahn, A. Biesdorf, G. Schotta, K. Rippe, and K. Rohr, "A spherical harmonics intensity model for 3d segmentation and 3d shape analysis of heterochromatin foci," Med. Image Anal. **32**, 18–31 (2016).